

# Highly effective Fe-N-C electrocatalysts toward oxygen reduction reaction originated from 2,6-diaminopyridine

**Weixiang Yang**

Southwest Petroleum University School of New Energy and Materials

**Shuihua Tang** (✉ [spraytang@hotmail.com](mailto:spraytang@hotmail.com))

Southwest Petroleum University <https://orcid.org/0000-0002-4097-7313>

**Qiankuan Huang**

Southwest Petroleum University School of New Energy and Materials

**Qian Zhang**

Southwest Petroleum University School of New Energy and Materials

**Zhen Tang**

Southwest Petroleum University School of New Energy and Materials

**Shuang Yang**

Southwest Petroleum University School of New Energy and Materials

---

## Research Article

**Keywords:** 2,6-Diaminopyridine, Fe-N<sub>x</sub> species, Oxygen reduction reaction, Fuel cell

**Posted Date:** March 5th, 2021

**DOI:** <https://doi.org/10.21203/rs.3.rs-269575/v1>

**License:** © ⓘ This work is licensed under a Creative Commons Attribution 4.0 International License.

[Read Full License](#)

---

**Version of Record:** A version of this preprint was published at Journal of Materials Science: Materials in Electronics on March 20th, 2021. See the published version at <https://doi.org/10.1007/s10854-021-05690-3>.

# Abstract

Fe-N-C electrocatalysts have been intensively studied due to their extraordinary catalytic activity toward oxygen reduction reaction (ORR). Here we prepare a Fe-N-C electrocatalyst through cost-effective and nontoxic precursors of 2,6-diaminopyridine (DAP) and  $\text{FeCl}_3$ , where iron ions react with DAP to form  $\text{Fe-N}_x$  species first, followed by polymerization and pyrolysis. X-ray diffraction patterns display no obvious  $\text{Fe}_2\text{O}_3$  peaks observed in the catalyst as the nominal content of iron addition is less than 10 wt%. X-ray photoelectron spectroscopy spectra indicate that the catalyst has rich pyridinic nitrogen, graphitic nitrogen and  $\text{Fe-N}_x$  species, which are considered as active sites for ORR. Therefore the catalyst demonstrates an excellent catalytic activity with an onset potential of about 0.96 V, half-wave potential of about 0.84 V, and a limiting current density of  $5.8 \text{ mA cm}^{-2}$ , better than commercial Pt/C catalyst in an alkaline medium. Furthermore its stability is also much more excellent than that of Pt/C. This work provides a strategy to synthesize universal M-N-C catalysts.

## Introduction

With increasing concerns on pollution of environment and shortage of fossil energy [1-3], clean hydrogen energy has attracted great attention worldwide.  $\text{H}_2\text{-O}_2$  fuel cell is a device to convert chemical energy of hydrogen and oxygen directly into electrical energy by electrochemical reactions. Among all reactions, oxygen reduction reaction (ORR) occurring at the cathode determines the whole process due to its sluggish kinetics. Therefore, to resolve the cathode problem, ORR catalysts with excellent catalytic activity are imperative [4-7]. Nowadays, the most widely used and efficient ORR catalysts are Pt-based electrocatalysts in an acidic medium. Due to high price and small reserve of precious metal Pt, large-scale applications of fuel cell-driven vehicles are limited. Therefore, scientists are devoted to developing various non-precious metal catalysts to replace Pt/C catalysts [8-10]. The non-precious metal catalysts currently studied are including transition metal nitrogen-carbon catalysts, nitrogen-doped carbon catalysts, metal oxide catalysts, metal nitride catalysts, metal carbide catalysts, and so on. It is found that transition metal nitrogen-carbon catalyst is the most promising alternative for the noble metal catalyst, especially the Fe-N-C catalyst. The Fe-N-C catalysts usually possess various types of N-C active sites and  $\text{Fe-N}_x$ , thus the catalyst delivers outstanding performances [11-14]. Bao et al [15] developed a novel method for one-pot direct synthesis of N-doped graphene via the reaction of tetrachloromethane with lithium nitride under mild conditions. The distinct electronic structure perturbation induced by the incorporation of nitrogen in the graphene network was observed for the first time by scanning tunneling microscopy. The nitrogen content varied in the range of 4.5-16.4% and enhanced catalytic activity was demonstrated in a fuel cell cathode oxygen reduction reaction. Raymond [16] discovered that cobalt phthalocyanine has the ability to catalyze the reduction of oxygen in alkaline media. This discovery opened up a new field for the research of fuel cell catalysts. Since then, non-precious metal macrocyclic molecular complexes have received widespread attention as oxygen reduction catalysts, and a large number of non-precious metal macrocyclic molecular complex catalysts have been developed [17-21]. Scientists have studied the performances of catalysts prepared with polypyrrole (PPy) [22-24], formamide [25], polythiophene (PTh)

[26], poly-3-methylthiophene (PMeT) [27] and dicyandiamide (DCD) [28] for oxygen reduction reaction. Zenelay's research group [29] attached PPy on a carbon support, and then deposited metal cobalt on the resulting carbon-supported PPy by the sodium borohydride reduction method, and obtained a transition metal-containing carbon-supported conductive polymer oxygen reduction catalyst. They found that after introducing metal cobalt, the oxygen reduction catalytic activity and stability of the carbon-supported conductive polymer catalyst have been greatly improved. In the  $\text{H}_2\text{-O}_2$  single cell test, the power density can reach  $240 \text{ mW cm}^{-2}$  in the 30-hour  $\text{H}_2\text{-O}_2$  cell stability test, and its performance is stable. Lv et al. [30] synthesized hydrogen-substituted graphdiyne (HsGDY) using tris[(trimethylsilyl)ethynyl] benzene, and then heated to  $900^\circ\text{C}$  in an ammonia atmosphere for one hour to prepare pyridinic-N selectively doped catalyst. The performance of the catalyst in an alkaline medium is better than that of commercial Pt/C catalyst. This study fully proved that pyridine nitrogen demonstrated ORR activity. Researchers such as Scherson [31-33] found that these transition metal macrocyclic complexes heat-treated at high temperature can greatly improve the catalytic activity and stability of these catalysts for oxygen reduction. Therefore, high temperature heat treatment provides a practical method for preparing high activity and high stability carbon-based oxygen reduction catalyst. Dodelet et al [34] prepared ORR catalysts by pyrolyzing Fe acetate or Fe porphyrin adsorbed on a synthetic carbon, which is made from the pyrolysis of perylene tetracarboxylic dianhydride between  $400$  and  $1000^\circ\text{C}$  in a  $\text{H}_2/\text{NH}_3/\text{Ar}$  atmosphere. They discovered that when Fe acetate was the Fe precursor,  $\text{FeN}_2/\text{C}$  may represent up to 80% of the catalytic sites, while this fell to a maximum of about 50% when Fe porphyrin was the precursor, and  $\text{FeN}_2/\text{C}$  was more electrocatalytically active than  $\text{FeN}_4/\text{C}$ .

In this manuscript, a high-performance Fe-N-C catalyst will be synthesized by pyrolysis of a polymer containing Fe-N<sub>x</sub> complex. Cost-effective and environmental-friendly 2,6-diaminopyridine (DAP) is used as monomer,  $\text{FeCl}_3$  is added to preform Fe-N complex with DAP, later DAP is polymerized. Eventually the polymer will be treated at elevated temperature, and the resulting catalyst will be characterized and tested.

## Experimental

### Preparation of Fe-N-C catalysts

1 mmol of DAP and specified amount of  $\text{FeCl}_3$  were dissolved in 30 mL of DI water, then 1 mmol of APS solution was added drop by drop, thus the polymer PDAP containing  $\text{Fe}^{3+}$  was synthesized, the polymerization reaction of Fe-DAP is shown in **Fig. 1**. Later the Fe-PDAP polymer will be filtrated and washed by DI water, till most of soluble small molecules,  $\text{Cl}^-$ , and free  $\text{Fe}^{3+}$  will be removed, and then the filter cake is dried and pulverized. After that, the polymer was heated to  $900^\circ\text{C}$  at a rate of  $5^\circ\text{C min}^{-1}$  and maintained for 1 h in a nitrogen flow. Eventually the Fe-N-C catalyst can be obtained. Fe contents of 2.5, 5, 7.5, 10 wt% (defined as mass ratio of Fe element to DAP) and pyrolysis times of 0.5, 1, 2 h were investigated, and the catalysts were denoted as Fe-N-C-900-mwt% and Fe-N-C-900-nh, respectively. For

comparison, Ni-N-C and Co-N-C catalysts were also prepared with the same parameters of synthesizing the Fe-N-C catalyst by using  $\text{NiCl}_2$  and  $\text{CoCl}_2$  as precursors, respectively.

### Physicochemical characterization

Thermogravimetric analysis (TGA) of Fe-PDAP mixtures was carried out from room temperature to 1000 °C in a  $\text{N}_2$  atmosphere at a heating rate of  $10\text{ }^\circ\text{C min}^{-1}$  on SDTA851e instrument. Transmission electron microscopy (TEM) was performed using a Libra 200FE microscope (Carl Zeiss SMT Pte Ltd) under an operating voltage of 200 keV. Powdered X-ray diffraction pattern (XRD) was recorded on an X'Pert Pro MPD diffractometer at a scan rate of  $5^\circ\text{ min}^{-1}$ . X-ray photoelectron spectroscopy (XPS) analysis was carried out on Thermo Scientific ESCALAB 250Xi X-ray photoelectron spectrometer with Al-K $\alpha$  source. The Brunauer-Emmett-Teller (BET) surface area was analyzed through  $\text{N}_2$  adsorption-desorption isotherms measured at 77 K on a Micromeritics ASAP-2460. Pore size distributions and average pore volume were calculated by BJH method.

### Electrochemical characterization

All the electrochemical measurements were performed on a rotating disk electrode in a typical three-electrode cell using electrochemical workstation (AutoLab Potentiostat 302N, Metrohm, Holland) at room temperature. The cell was composed of a glassy carbon as a working electrode (GC, 5 mm in diameter),  $\text{HgO}/\text{Hg}$  (0.1 M KOH) as a reference electrode and a platinum wire as a counter electrode. The catalyst ink was prepared by mixing 5 mg of catalysts, 48  $\mu\text{L}$  of 5 wt% Nafion® solution (Du Pont), and 1 mL of ethanol after sonication for 30 minutes. Then the catalyst ink was dropped onto the glassy carbon electrode and the loading was controlled at  $1.2\text{ mg cm}^{-2}$ . For comparison, 40 wt% Pt/C (Johnson Matthey) was made same as above with a Pt loading of  $25\text{ }\mu\text{g cm}^{-2}$ . Both cyclic voltammetry (CV) and linear sweep voltammetry (LSV) were performed in 0.1 M KOH solution. All potentials related to electrochemical tests in the context are referred to a reversible hydrogen electrode (RHE). The Koutecky-Levich equation can be used to express the current density generated by the reaction at a certain potential. In the RDE test, when the reaction reaches the limit diffusion control on the electrode surface, the concentration of the reactant on the electrode surface is zero and does not change with time. The expression of the rotating disk electrode is obtained as follows: **see formula 1 in the supplementary files.**

Where  $j$  is the measured current density ( $\text{mA}/\text{cm}^2$ ),  $j_k$  is the kinetic current density ( $\text{mA}/\text{cm}^2$ ),  $j_\infty$  is the limiting current density ( $\text{mA}/\text{cm}^2$ ),  $\omega$  is the angular velocity of the electrode rotation (rpm),  $n$  is the number of electrons reduced by an oxygen molecule.  $F$  is Faraday's constant ( $96487\text{ C mol}^{-1}$ ),  $C_0$  is concentration of oxygen in the electrolyte ( $1.117\text{ E}^{-6}\text{ mol mL}^{-1}$ ),  $D$  is diffusion coefficient for oxygen in the electrolyte ( $1.9\text{ E}^{-5}\text{ cm}^2\text{ s}^{-1}$ ),  $\nu$  is the kinematic viscosity of the electrolyte ( $0.01\text{ cm}^2\text{ s}^{-1}$  for 0.1 M KOH). The K-L diagram ( $j^{-1}$  vs.  $\omega^{-1/2}$ ) can be drawn from the current density measured at different speeds, and the electron transfer number  $n$  is calculated according to the above formula to further explore the mechanism of the oxygen reduction reaction. In order to investigate the ORR activities of the catalysts, the polarization plots are

recorded in 0.1 M KOH oxygen-saturated solution at a rotation rate of 1600 rotation per minute (rpm) and the stability test was carried out at 0.6 V vs RHE for 3 h by chronoamperometry method.

## Results And Discussion

As schematically illustrated in **Fig. 2**, when DAP and  $\text{FeCl}_3$  solution are dissolved in DI water, concurrently Fe and DAP may form a complex to obtain Fe-DAP containing Fe-N species, then Fe-DAP complex will be polymerized to form Fe-PDAP. Later Fe-PDA will be filtrated and washed by DI water, thus most of soluble small molecules,  $\text{Cl}^-$ , and free  $\text{Fe}^{3+}$  will be removed. After the filter cake is dried and pulverized, it will be treated at elevated temperature in nitrogen flow. Eventually the Fe-N-C catalyst can be prepared. Because only trace of  $\text{Fe}^{3+}$  remains in the power, so the carbonization may be not very complete during the pyrolysis process.

**Fig. 3** displays the mass loss of Fe-PDAP tested by thermogravimetric analysis (TG) and corresponding differential thermogravimetric analysis (DTG) in  $\text{N}_2$  flow. We can see that the pyrolysis process of Fe-PDAP can be mainly divided into three stages. The first starts at 40 °C and reaches a plateau at about 180 °C, with an associated mass loss of 19%, which can be assigned to the volatilization of absorbed water [35,36]. The second step, from 180 to 420 °C, shows a mass loss of 20%, which might be related to the cleavage of C-N bond of pyridine C-NH<sub>2</sub> group in PDAP as well as some polymers with low molecular weight. With temperature further increasing, the third stage shows that the PDAP is gradually carbonized and transformed. For example, all of hydrogen and the rest of polymers with low molecular weight will get removed, and the polymers with medium and high molecular weights will be transformed into active sites such as pyridinic-N, graphitic-N, and Fe-N<sub>x</sub>. From 500 to 1000 °C, we can see that the weight loss is occurring without a plateau, this may be ascribed to no additional Fe species existing for the carbonization procedure, because except for the  $\text{Fe}^{3+}$  forming the Fe-N<sub>x</sub> complex with DAP, the rest of  $\text{Fe}^{3+}$  has been washed after the polymerization process. One  $\text{Fe}^{3+}$  could form Fe-N<sub>x</sub> complex by combining with pyridine nitrogen in the DAP, because the nitrogen atom has lone-pair electron which can enter the outer orbital of Fe ion. From here we can deduce that the iron will be uniformly distributed in the following polymer and carbonized product due to the preformed Fe-N<sub>x</sub> complex; furthermore the Fe element could also exist in a separate single atom state in the Fe-N-C catalyst.

The XRD patterns of Fe-N-C catalysts with various Fe contents, standard patterns of graphite and  $\text{Fe}_2\text{O}_3$  are shown in **Fig. 4**. The diffraction peaks at 26° and 43° are characteristic planes of (002) and (101) of graphitized carbon. The strong peak (002) indicates that the carbon material in the Fe-N-C catalyst has relatively high degree of graphitization [37]. With increasing Fe content, an obviously characteristic peak corresponding to the crystal plane (110) of  $\text{Fe}_2\text{O}_3$  [38,39] appears at 35.6° for the Fe-N-C-10wt% sample, this indicates that there are still considerably free  $\text{Fe}^{3+}$  encapsulated in the polymer after washing by DI water, the  $\text{Fe}^{3+}$  ions convert into  $\text{Fe}_2\text{O}_3$  particles in the following carbonization procedure.

As shown in **Fig. 5**, it can be seen that the nitrogen adsorption-desorption curve is a typical type IV isotherm with an H3 hysteresis loop, so Fe-N-C-5wt% is a mesoporous carbon material with specific surface area as high as  $1279 \text{ m}^2 \text{ g}^{-1}$ , measured by Brunauer-Emmett-teller (BET) method[40]. The curve of pore size distribution confirms the mesoporous state, that the catalyst mainly shows an average pore diameter of about 2.5 nm, with BJH Adsorption cumulative volume of  $0.342 \text{ cm}^3 \text{ g}^{-1}$ . The large specific surface area and pore volume will provide more sufficient reaction sites for the gas-liquid-solid three-phase reaction and facilitate the mass transportation process.

TEM images of Fe-N-C-5wt% are shown in **Fig. 6**. We can see that the catalyst is composed of small and uniform particles with graphitized carbon fringes, and no obvious  $\text{Fe}_2\text{O}_3$  and other metal particles are observed. Combined with above XRD pattern, we don't see obvious diffraction peaks of Fe and its compounds, indicating that Fe element may be presented in a form of single atom. The graphitized stripes of carbon at the edge of the catalyst are in consistent with the graphitized carbon peak in the XRD pattern.

The composition and binding energy of the Fe-N-C catalyst are analyzed by XPS, as shown in **Fig. 7**. The Fe-N-C catalyst is mainly composed of elements of C, O, and N, only trace of Fe is observed. The contents of carbon, oxygen, nitrogen, and iron are 85.7, 9.4, 4.5, and 0.4 wt%, respectively. N can be mainly divided into four categories, as well-known pyridinic N (398.5 eV), pyrrolic N or Fe-N (399.2 eV), graphitic N (401.2 eV), and oxidized N (402.2 eV) [41,42]. From Fig. 7(c), the N 1s spectrum in the Fe-N-C catalyst consists of graphite-N, pyridine-N, Fe-Nx, and oxidized N, with respective mass proportions of 39%, 26%, 10%, and 25%. According to literature [43-45], graphite-N, pyridine-N, and Fe-Nx are considered as the active sites for an oxygen reduction reaction, so we can predict that the catalyst could possess excellent ORR activity. XPS spectrum of Fe 2p in **Fig. 7(c)** demonstrates that Fe exists in the forms of  $\text{Fe}^{2+}$  and  $\text{Fe}^{3+}$  [46-48], correlating the N information, we can deduce that Fe might be in the form of Fe-Nx.

The ORR performances of different catalysts are evaluated on a rotating disk electrode (RDE) in  $0.1 \text{ mol L}^{-1}$  KOH  $\text{O}_2$ -saturated solution at a rotation rate of 1600 rpm. Firstly different pyrolysis temperatures are investigated, for example 800 °C, 850 °C, 900 °C and 950 °C, the LSV curves are shown in **Fig. 8(a)**. We can see that pyrolysis temperature has great important influence on the ORR activity; the Fe-N-C-900-5wt% exhibits much better catalytic activity than Fe-N-C-800-5wt%. However, when the temperature increases to 1000 °C, the polymer is decomposed completely, later we will try the pyrolysis temperature of 950 °C. Later the effect of pyrolysis time on catalyst performance is tested and shown in **Fig. 8(b)**. As the pyrolysis time increases, the ORR performance increases and then decreases, one hour is the optimum time. This may be due to shorter time leading insufficient carbonization, and longer time decreasing the specific surface. Different mass ratios of nominal Fe to DAP (2.5:100, 5:100, 7.5:100, and 10:100) are further investigated; the catalysts are denoted as Fe-N-C-900-2.5wt%, Fe-N-C-900-5wt%, Fe-N-C-900-7.5wt%, and Fe-N-C-900-10, respectively. Their ORR activities are shown in **Fig. 8(c)**, the ORR performance increases with iron content firstly, and the Fe-N-C-900-5wt% catalyst demonstrates the most positive on-set potential, half-wave potential and biggest limiting current density; then decreasing with Fe content.

This reason is that lower Fe content cannot form enough Fe-N<sub>x</sub> active sites, but more Fe content may influence the DAP polymerization and following carbonization process.

We know that Fe, Co, and Ni are all carbonization catalysts and Fe-N<sub>x</sub>, Co-N<sub>x</sub>, and Ni-N<sub>x</sub> species are active sites for ORR. Therefore, the ORR activity of Fe-N-C-900-5wt%, Co-N-C-900-5wt%, and Ni-N-C-900-5wt% are investigated and compared with commercial Pt/C catalysts (40 wt%, from Johnson Matthey). As shown in **Fig. 8(d)**, the sequence in ORR activity is Fe-N-C-900-5wt% @ Pt/C (JM) > Co-N-C-900-5wt% > Ni-N-C-900-5wt%. We can see that the ORR activity of Fe-N-C catalyst is comparable to that of Pt/C catalyst, and is much better than those of Co- and Ni-based catalysts.

In order to study the reaction mechanism, we carried out linear sweep tests at different rotation rates. As shown in **Fig. 8(e)**, the limiting current density increases with rotation rates, while the onset potential remains unchanged. **Fig. 8(f)** is the Koutecky-Levich (K-L) plots of Fe-N-C, which shows very good linearity at different potentials. According to the K-L plots, the numbers of electron transfer per oxygen molecule during the oxygen reduction reaction at different potentials (0.6-0.3 V) is calculated to be 3.6-3.99. This indicates that the Fe-N-C catalyst mainly undergoes a four-electron oxygen reduction process in alkaline media.

Cyclic voltammetry and Chronoamperometry methods are used to evaluate the stability of Fe-N-C-900-5wt% and commercial Pt/C catalysts, respectively. From **Fig. 9(a-b)**, after scanning at sweep rate of 50 mV s<sup>-1</sup> for 1000 cycles, the intrinsic catalytic activity of Fe-N-C-900-5wt% exhibits almost no change, only the limiting current density reduces slightly, indicating mass transportation becomes less easy; However, for Pt/C catalyst, the catalytic activity and limiting current density decrease, and the half-wave potential drops nearly 30 mV. If Chronoamperometry is running at 0.6 V (vs RHE) for 3 hours, the current retention of Fe-N-C-900-5wt% is 94%, while only 52% for Pt/C, as shown in **Fig. 9(c)**. We can draw a conclusion that the stability of Fe-N-C-900-5wt% catalyst is much better than Pt/C in an alkaline medium. Furthermore, whether the ORR activity or the stability, the Fe-N-C-900-5wt% catalyst shows better performance than Pt/C catalyst. It can be seen from **Table 1** that under alkaline conditions, the catalytic performance of Fe-N-C-900-5wt% catalyst is comparable to the similar Fe-N-C catalysts.

**Table 1** Comparison of ORR performances of related Fe-N-C electrocatalysts and Fe-N-C-900-5wt% in O<sub>2</sub>-saturated 0.1 mol/L KOH solution.

Catalysts	$E_{\text{onset}}$ (V vs RHE)	$E_{1/2}$ (V vs RHE)	$J_{\text{lim}}$ (mA cm <sup>-2</sup> )	References
Fe-N/C	0.892	0.761	~4.26	[49]
Fe-N/C	0.93	0.801	~5.6	[50]
Fe-A-RGO	0.83	0.69	~5.8	[51]
Fe-N/C	0.94	0.81	~4.7	[52]
Fe-N-C	0.91	0.814	~4.6	[53]
Fe/N/C	0.939	0.739	~5.3	[54]
Fe-N-C-NH <sub>3</sub>	0.98	0.85	5.1	[55]
Fe-N-C-900-5wt%	0.96	0.84	5.8	This Work

## Conclusions

Fe-N-C catalyst with single-atom iron distributed has been successfully synthesized by pyrolysis of PDAP containing preformed Fe-N<sub>x</sub> complex. XRD pattern and TEM images confirm that iron atoms are uniformly distributed in the Fe-N-C-900-5wt% catalyst without Fe<sub>2</sub>O<sub>3</sub> or other Fe-containing crystalline. The Fe-N-C catalyst demonstrates best ORR activity and stability when control the pyrolysis temperature at 900 °C and last for 1 hour with nominal Fe content of 5 wt%. The Fe-N-C-900-5wt% catalyst exhibits comparable ORR activity and much better stability with respect to commercial Pt/C catalyst in an alkaline medium. This can provide a strategy to synthesize single-atom distributed catalysts and apply cheap and nontoxic C and N precursor to prepare high-efficient ORR catalyst for alkaline fuel cells.

## References

- [1] M.A.Z.G. Sial, M.A.U. Din, X. Wang, Chem. Soc. Rev. 47, 6175-200 (2018)
- [2] M.L. Pegis, C.F. Wise, D.J. Martin, J.M. Mayer, Chem. Rev. 118, 2340-91 (2018)
- [3] A. Kulkarni, S. Siahrostami, A. Patel, J.K. Norskov, Chem. Rev. 118, 2302-12 (2018)
- [4] K. Jiang, S. Back, A.J. Akey, C. Xia, Y. Hu, W. Liang, D. Schaak, E. Stavitski, J.K. Norskov, S. Siahrostami, H. Wang, Nat. Commun. 10, 3397 (2019)
- [5] F. Xiao, G.-L. Xu, C.-J. Sun, M. Xu, W. Wen, Q. Wang, M. Gu, S. Zhu, Y. Li, Z. Wei, X. Pan, J. Wang, K. Amine, M. Shao, Nano Energy. 61, 60-8 (2019)
- [6] X. Sun, S. Sun, S. Gu, Z. Liang, J. Zhang, Y. Yang, Z. Deng, P. Wei, J. Peng, Y. Xu, C. Fang, Q. Li, J. Han, Z. Jiang, Y. Huang, Nano Energy. 61, 245-50 (2019)



- [7] Z. Liang, W. Guo, R. Zhao, T. Qiu, H. Tabassum, R. Zou, *Nano Energy*. 64, 103917 (2019)
- [8] G. Han, Y. Zheng, X. Zhang, Z. Wang, Y. Gong, C. Du, M.N. Banis, Y.-M. Yiu, T.-K. Sham, L. Gu, Y. Sun, Y. Wang, J. Wang, Y. Gao, G. Yin, X. Sun, *Nano Energy*. 66, 104088 (2019)
- [9] Z. Chen, W. Gong, Z. Liu, S. Cong, Z. Zheng, Z. Wang, W. Zhang, J. Ma, H. Yu, G. Li, W. Lu, W. Ren, Z. Zhao, *Nano Energy*. 60, 394-403 (2019)
- [10] S. Chen, N. Zhang, C.W.N. Villarrubia, X. Huang, L. Xie, X. Wang, X. Kong, H. Xu, G. Wu, J. Zeng, H.-L. Wang, *Nano Energy*. 66, 104164 (2019)
- [11] D. Zhao, Z. Zhuang, X. Cao, C. Zhang, Q. Peng, C. Chen, Y. Li, *Chem. Soc. Rev.* 49, 2215-64 (2020)
- [12] K. Kumar, L. Dubau, M. Mermoux, J. Li, A. Zitolo, J. Nelayah, F. Jaouen, F. Maillard, *Angew. Chem. Int. Ed.* 59, 3235-3243 (2020)
- [13] T. Sharifi, E. Gracia-Espino, A. Chen, G. Hu, T. Wagberg, *Adv. Mater.* 10, 1902084 (2020)
- [14] G. Chen, P. Liu, Z. Liao, F. Sun, Y. He, H. Zhong, T. Zhang, E. Zschech, M. Chen, G. Wu, J. Zhang, X. Feng, *Adv. Mater.* 32, 1907399 (2020)
- [15] D.H. Deng, X. L. Pan, L. A.Yu,Y.P. Jiang, J. Qi, W.X. Li, Q. Fu, X. Ma, Q.K. Xue, G.Q. Sun, X.H. Bao, *Chem. Mater.* 23(5), 1188-1193 (2011)
- [16] R.Jasinski, *Nature* 201,1212-1213 (1964)
- [17] X.L. Li, H.L. Wang, J.T. Robinson, H. Sanchez, G. Diankov, H.J. Dai, *J. Am. Chem. Soc.* 131, 15939-44 (2009)
- [18] L.P. Zhang, J.B. Niu, L. Dai, Z.H. Xia, *Langmuir*. 28, 7542-50 (2012)
- [19] Z.H. Sheng, L. Shao, J.J. Chen, W.J. Bao, F.B. Wang, X.H. Xia, *ACS Nano*. 5, 4350-8 (2011)
- [20] S.Y. Wang, L.P. Zhang, Z.H. Xia, A. Roy, D.W. Chang, J.B. Baek, L.M. Dai, *Angew. Chem. Int. Ed.* 51, 4209-12 (2012)
- [21] X. Liu, L. Li, C.G. Meng, Y. Han, *J. Phys. Chem. C*. 116, 2710-9 (2012)
- [22] F.L. Meng, Z.L. Wang, H.X. Zhong, J. Wang,J.M. Yan,X.B. Zhang, *Adv. Mater.* 28, 7948–7955 (2016)
- [23] Z.Y. Wu, X.X. Xu, B.C. Hu, H.W. Liang, Y. Lin, L. F. Chen, S. H.Yu, *Angew. Chem. Int. Ed.* 51, 8179-8183 (2015)
- [24] J. Yang, X. Wang, B. Li, L. Ma, L. Shi, Y.J. Xiong, H.X. Xu, *Adv. Funct.Mater.* 27, 1606497 (2018)

- [25] G. Zhang, Y. Jia, C. Zhang, X. Xiong, K. Sun, R. Chen, W. Chen, Y. Kuang, L. Zheng, H. Tang, W. Liu, J. Liu, X. Sun, W. Lin, H. Dai, *Energy Environ. Sci.* 12, 1317-1325 (2019)
- [26] Q. Li, W. Chen, H. Xiao, Y. Gong, Z. Li, L. Zheng, X. Zheng, W. Yan, W.-C. Cheong, R. Shen, N. Fu, L. Gu, Z. Zhuang, C. Chen, D. Wang, Q. Peng, J. Li, Y. Li, *Adv. Mater.* 30, 1800588 (2018)
- [27] V. G. Khomenko, V. Z. Barsukov, A. S. Katashinskii, *Electrochim. Acta.* 50(7-8), 1675-1683 (2005)
- [28] J. Wang, H. Wu, D. Gao, S. Mao, G. Wang, X. Bao, *Nano Energy.* 13, 387-396 (2015)
- [29] R. Bashyam, P. Zelenay, *Nature.* 443 63-6 (2006)
- [30] Q. Lv, W. Si, J. He, L. Sun, C. Zhang, N. Wang, Z. Yang, X. Li, X. Wang, W. Deng, Y. Long, C. Huang, Y. Li, *Nat. Commun.* 9, 3376 (2018)
- [31] H. Meng, F. Jaouen, E. Proietti, M. Lefevre, J.P. Dodelet, *Electrochem Commun.* 11, 1986-9 (2009)
- [32] J. Liu, X.J. Sun, P. Song, Y.W. Zhang, W. Xing, W.L. Xu, *Adv. Mater* 25, 6879-83 (2013)
- [33] C.H. Choi, S.H. Park, S.I. Woo, *Appl. Catal. B-Environ.* 119, 123-31 (2012)
- [34] E.J. Biddinger, D. von Deak, U.S. Ozkan. *Top Catal.* 52, 1566-74 (2009)
- [35] Y. Deng, H. Huangfu, S. Tang, J. Li, *Chin. J. Catal.* 38, 1668-1679 (2017)
- [36] Y. Li, Q. Shen, R. Guan, J. Xue, X. Liu, H. Jia, B. Xua, Y. Wu, *J. Mater. Chem. C.* 8, 1025 (2020)
- [37] R.F. Wang, H. Wang, H. Li, W. Wang, J.L. Key, L. Khotseng, S. Ji, *Electrochim. Acta.* 132, 251-7 (2014)
- [38] Q. G. He, X. F. Yang, R. H. He, A. Bueno-Lopez, H. Miller, X. M. Ren, W. L. Yang, B. E. Koel, *J Power Sources.* 213, 169-79 (2012)
- [39] F. F. Liu, H. L. Peng, C. H. You, Z. Y. Fu, P. Y. Huang, H. Y. Song, S. J. Liao, *Electrochim. Acta.* 138, 353-9 (2014)
- [40] B. Zhong, L. Zhang, J. Yu, K. Fan, *J. Colloid Interface Sci.* 546, 113-121 (2019)
- [41] K. Singh, F. Razmjooei, J. S. Yu, *J. Mater. Chem. A.* 5, 20095-119 (2017)
- [42] S. Gong, C. Wang, P. Jiang, L. Hu, H. Lei, Q. Chen, *J. Mater. Chem. A.* 6, 13254-62 (2018)
- [43] Y. He, S. Hwang, D. A. Cullen, M. A. Uddin, L. Langhorst, B. Li, S. Karakalos, A. J. Kropf, E.C. Wegener, J. Sokolowski, M. Chen, D. Myers, D. Su, K. L. More, G. Wang, S. Litster, G. Wu, *Energy Environ. Sci.* 12, 250-60 (2019)

- [44] Y. Yang, K. Mao, S. Gao, H. Huang, G. Xia, Z. Lin, P. Jiang, C. Wang, H. Wang, Q. Chen, *Adv. Mater.* 30, 1801732 (2018)
- [45] J. Han, H. Bao, J. Q. Wang, L. Zheng, S. Sun, Z. L. Wang, C. Sun, *Appl. Catal. B-Environ.* 280, 119411 (2021)
- [46] Z. Li, Z. Zhuang, F. Lv, H. Zhu, L. Zhou, M. Luo, J. Zhu, Z. Lang, S. Feng, W. Chen, L. Mai, S. Guo, *Adv. Mater.* 30, 18003220 (2018)
- [47] C. Zhu, Q. Shi, B. Z. Xu, S. Fu, G. Wan, C. Yang, S. Yao, J. Song, H. Zhou, D. Du, S.P. Beckman, D. Su, Y. Lin, *Adv. Energy Mater.* 8, 1801956 (2018)
- [48] E. Hu, X. Y. Yu, F. Chen, Y. Wu, Y. Hu, X. W. Lou, *Adv. Energy Mater.* 8, 1702476 (2018)
- [49] Q. Wu, D. Deng, Y. He, Z. Zhou, S. Sang, Z. Zhou, *J. Cent. South Univ.* 27, 344–355 (2020)
- [50] T. Wu, Y. Li, Y. Li, J. Hong, H. Wu, J. Mao, Y. Wu, Q. Cai, C. Yuan, L. Dai, *Nanotechnology.* 30, 305402 (2019)
- [51] W. Sudarsono, W. Y. Wong, K. S. Loh, E. H. Majlan, N. Syarif, K. Y. Kok, R. M. Yunus, K. L. Lim, I. Hamada, *Int. J. Hydrogen. Energy.* 45, 23237-23253 (2020)
- [52] Yi Zhang, N. Wang, N. Jia, J. Wang, J. Sun, F. Shi, Z.H. Liu, R. Jiang, *Adv. Mater. Interfaces*, 6, 1900273 (2019)
- [53] G. A. Ferrero, N. Diez, M. Sevilla, A. B. Fuertes, *Microporous Mesoporous Mater.* 278, 280-288 (2019)
- [54] M. Guo, L. Wang, Y. Gao, G. Li, *Int. J. Hydrogen. Energy.* 44, 3625-3635 (2019)
- [55] Z. Chen, D. Zhao, C. Chen, Y. Xu, C. Sun, K. Zhao, M.A. Khan, D. Ye, H. Zhao, J. Fang, X. A. Sun, J. Zhang, *J. Colloid Interface Sci.* 582, 1033-1040 (2021)

## Figures

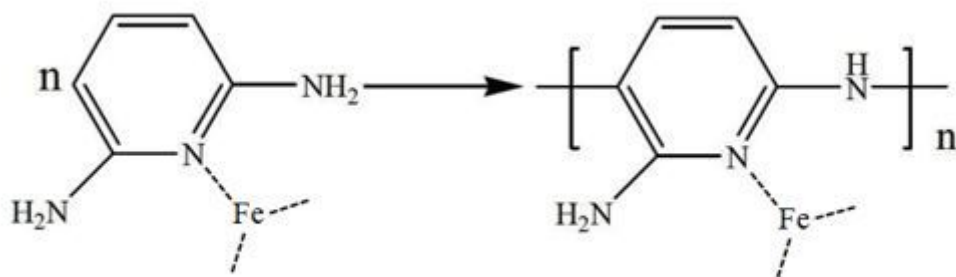


Figure 1

Polymerization reaction of Fe-DAP to Fe-PDAP.

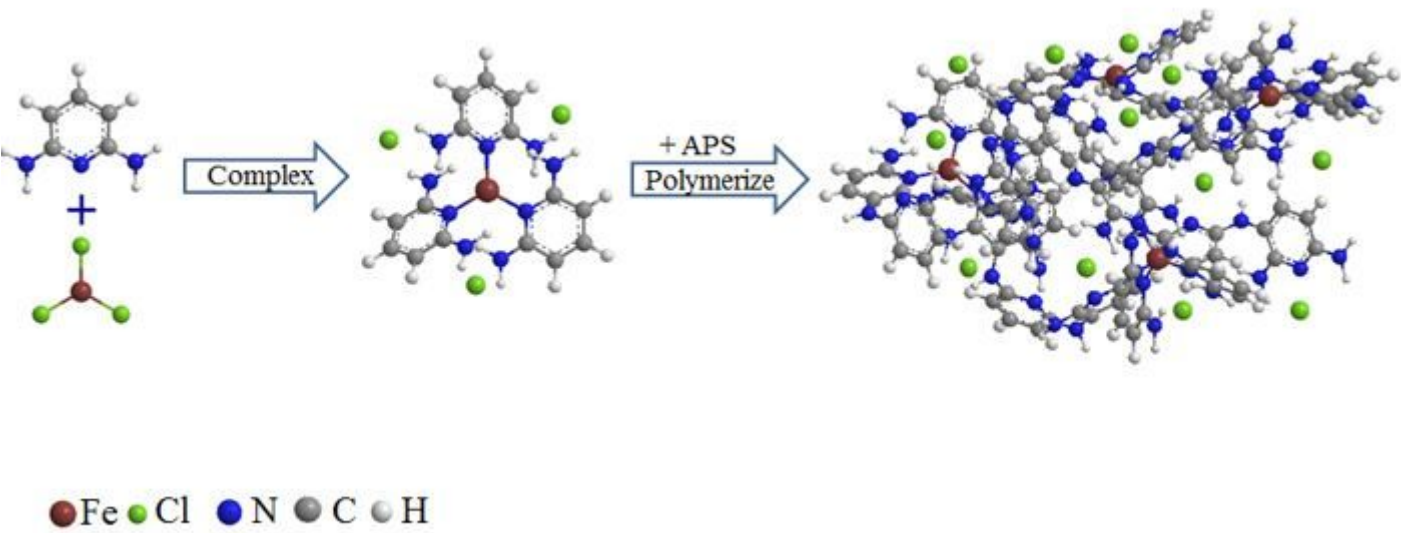


Figure 2

Schematic illustration of polymerization process of Fe-PDAP complex.

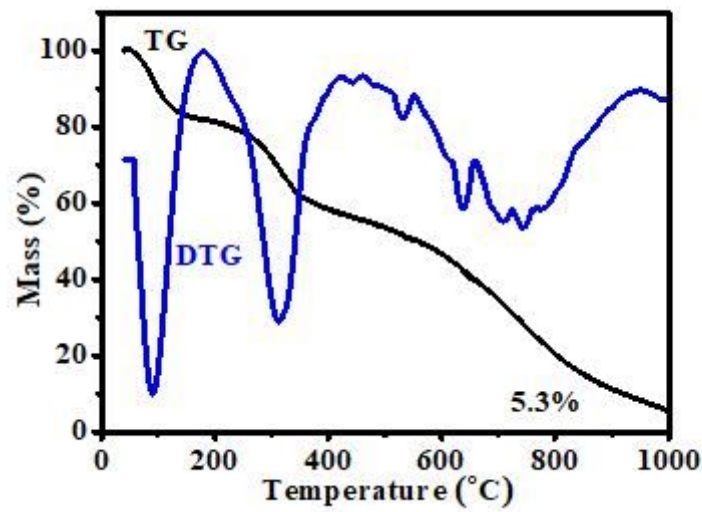


Figure 3

TG and DTG plots of Fe-PDAP at heating rate of 10 °C min<sup>-1</sup> in N<sub>2</sub> flow.

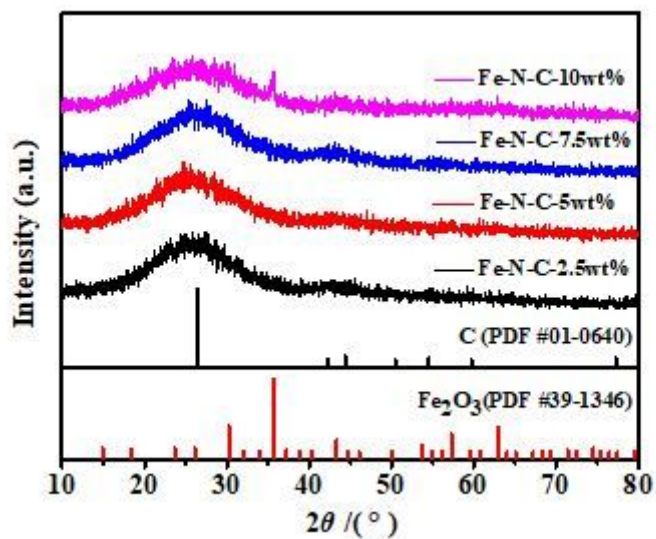


Figure 4

XRD patterns of Fe-N-C catalysts with various Fe contents, standard patterns of graphite and  $\text{Fe}_2\text{O}_3$ .

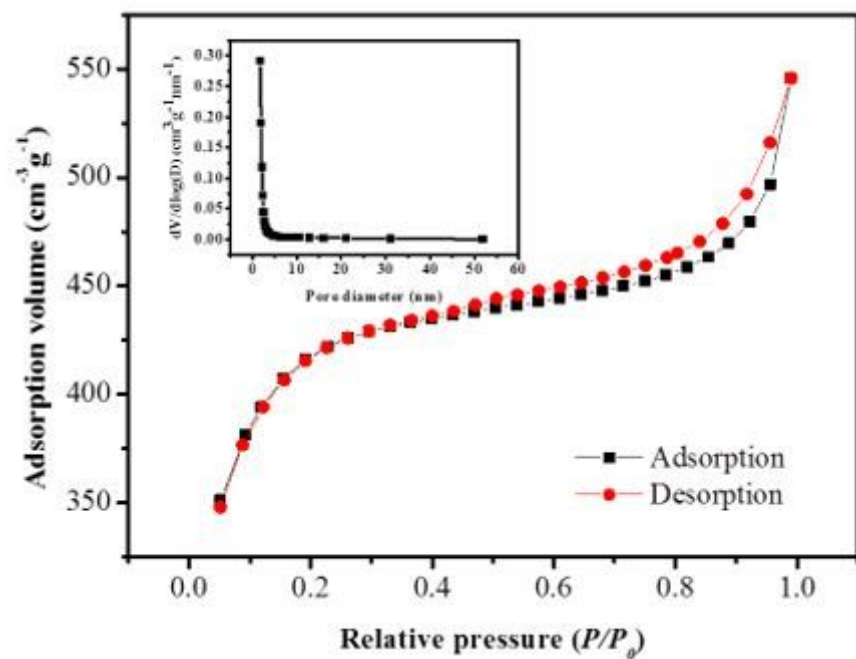


Figure 5

$\text{N}_2$  adsorption-desorption isotherm of Fe-N-C-5wt%, inset is the corresponding pore size distribution.

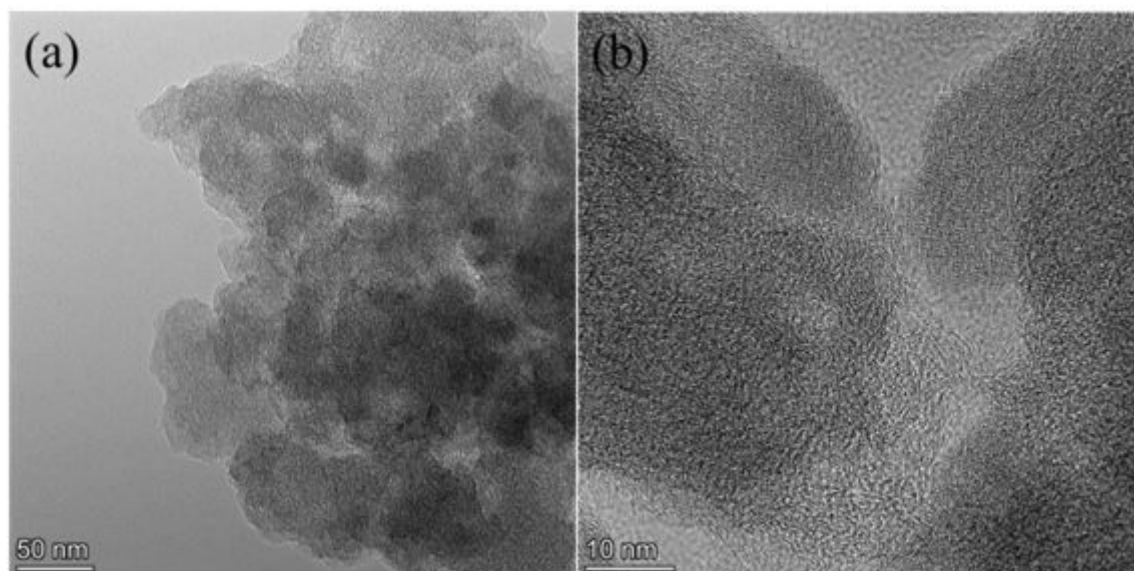


Figure 6

TEM images of Fe-N-C-900-5wt%.

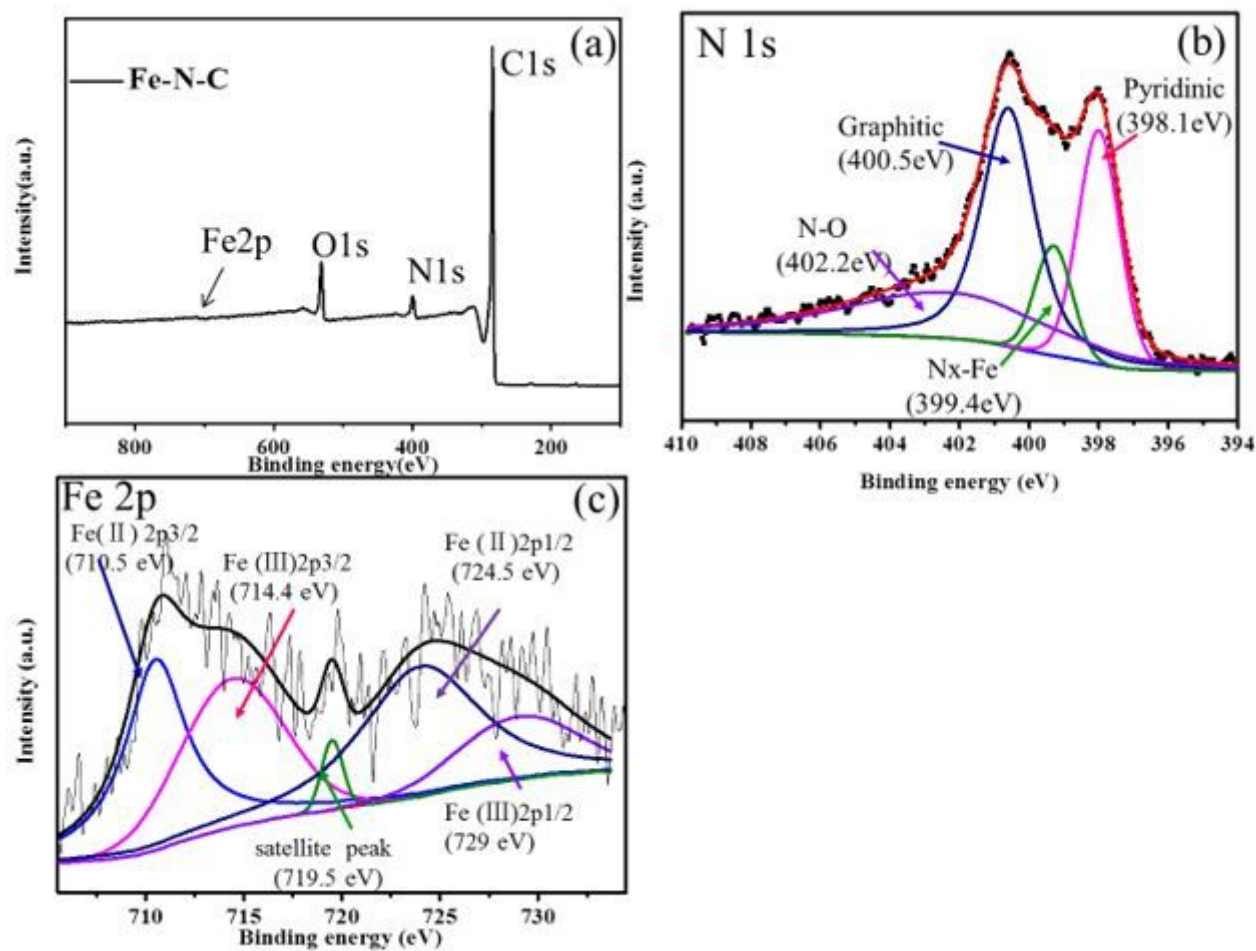


Figure 7



(a) XPS survey of Fe-N-C-5wt%, High-resolution spectra of (b) N1 s and (c) Fe 2p of Fe-N-C-5wt%.

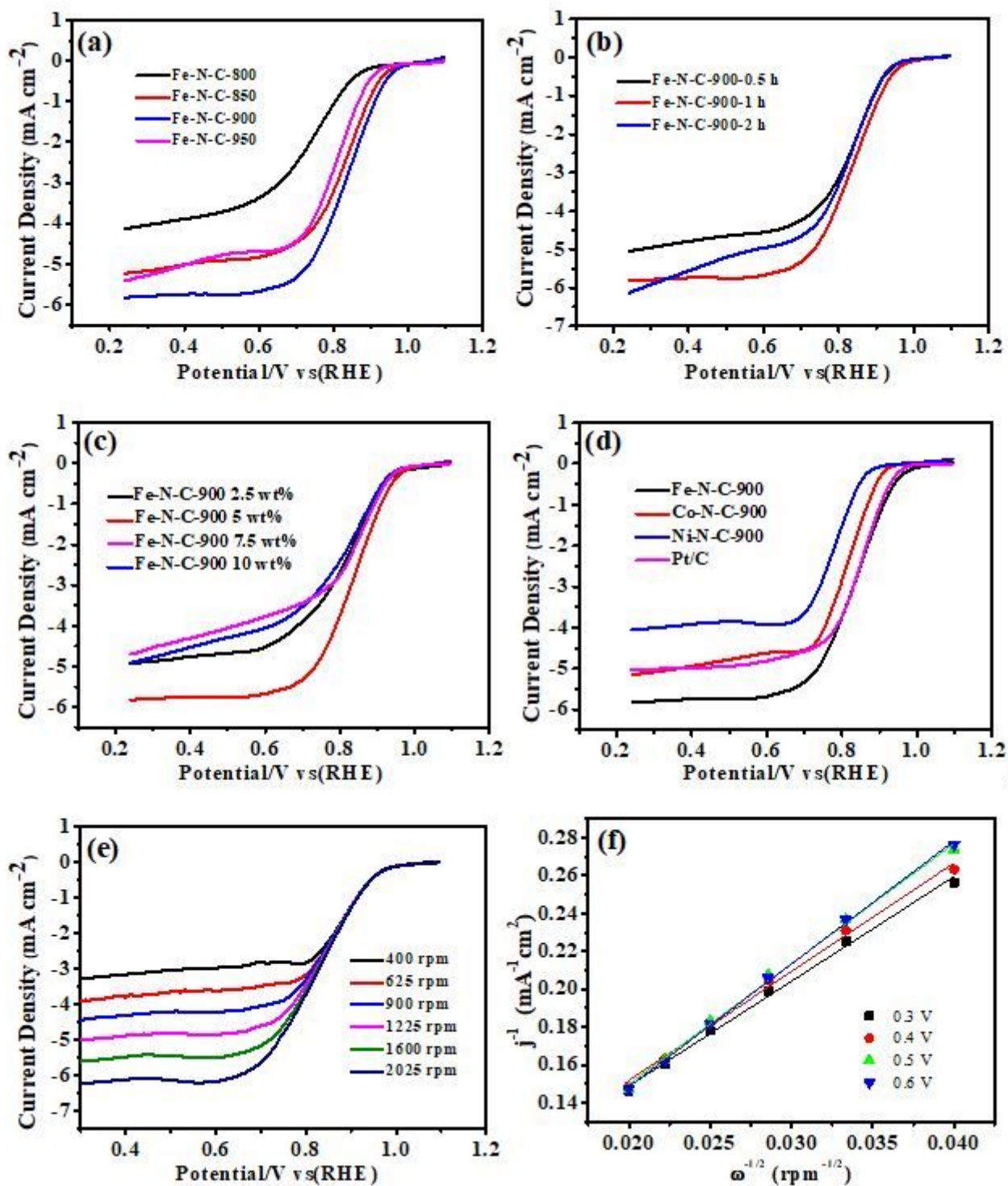
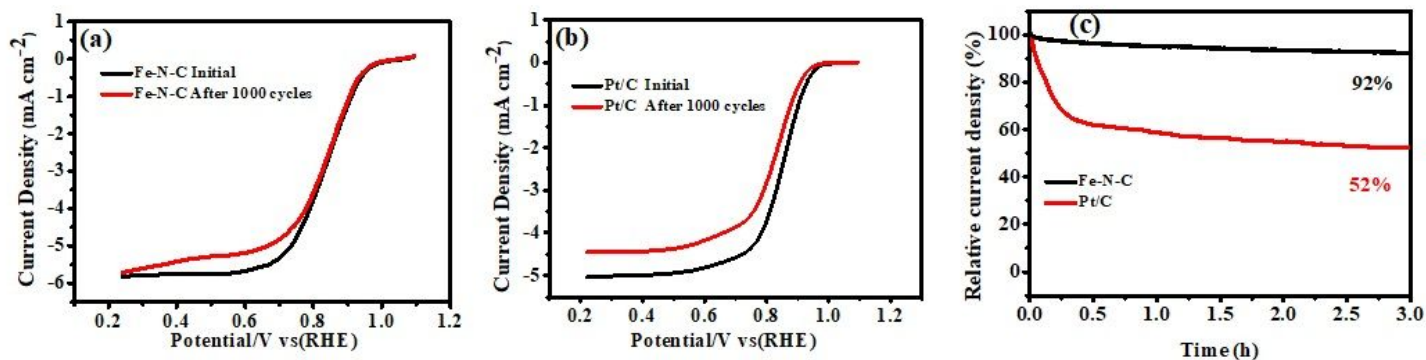


Figure 8

LSV curves of (a) Fe-N-C catalysts at different pyrolysis temperatures; (b) Fe-N-C-900-5wt% for different pyrolysis time; (c) Fe-N-C-900 catalysts with different nominal content of Fe; and (d) Fe-N-C-5wt%, Co-N-C-5wt%, Ni-N-C-5wt% and Pt/C catalysts in 0.1 mol L<sup>-1</sup> O<sub>2</sub>-saturated KOH solution at a rotation rate of 1600 rpm. (e) LSV curves at different rotation rates and (f) K-L plots of Fe-N-C.



**Figure 9**

LSV curves of (a) Fe-N-C-900-5wt% and (b) commercial Pt/C catalysts before and after 1000 CV cycles, (c) Chronoamperometric responses of the Fe-N-C and Pt/C catalysts at 0.6 V (vs RHE) in an  $\text{O}_2$ -saturated 0.1 mol L<sup>-1</sup> KOH solution.

## Supplementary Files

This is a list of supplementary files associated with this preprint. Click to download.

- [formula.docx](#)